Online ISSN: 2981-0396 Print ISSN: 2981-0388

International Journal of Iron & Steel Society of Iran

Journal Homepage: https://journal.issiran.com/

Research Article

Effects of CeO_2 Flux and Shielding Gas In A-TIG Welding on The Microstructure, Corrosion and Passive Film of Super Duplex Phase Stainless Steel 2507

M. Goliani [1], A. R. Ebrahimi *[2]

Department of Materials and Metallurgical Engineering, Amirkabir University of Technology, Tehran, Iran

ARTICLE INFO

Keywords:

Super-Duplex Stainless Steel 2507, Active TIG Welding, Cerium Oxide Flux, Corrosion, Shielding Gas, Microstructure, Passive Film.

Article history:

Received 11 May 2024
Received in revised form 21 August 2024
Accepted 26 November 2024

ABSTRACT

This study explores using CeO_2 flux with Ar and Ar+5%N_2 shielding gases to enhance the welding process of 2507 super duplex stainless steel through active TIG welding. It discusses their impact on weld geometry, microstructure, pitting corrosion, and passive film in a 3.5% NaCl solution, using scanning electron microscopy, cyclic polarization curves, electrochemical impedance spectroscopy, and Mott-Schottky analysis. The results indicate that the proportion of austenite phase in the microstructure resulting from A-TIG welding with CeO_2 flux and Ar gas increased to 49.1%, compared to 42.1% in conventional TIG welding, aligning well with the phase balance in the base metal. The microstructure of A-TIG welding with cerium oxide flux and shielding gas mixture, with increased austenite with quasi-spherical shapes, has created a morphology similar to the base metal. When utilizing CeO_2 flux for welding in conjunction with a shielding gas mixture, a significant reduction in grain size occurs, which becomes about four times smaller than the base metal. Moreover, it modifies the shape, size, and distribution of inclusions. This increased corrosion resistance and significantly reduced I_{corr} and I_{pass} by approximately 22 times. Additionally, EIS and Mott-Schottky tests indicated decreased point defects in the passive film and a greater propensity to form a dense protective film with higher chemical stability in A-TIG welding, mainly when using a shielding gas mixture. These findings demonstrate the crucial role of cerium in enhancing the welding of super duplex stainless steel, potentially representing a significant breakthrough in the industry.

1. Introduction

Duplex stainless steels (DSS) consist of a ferrite-austenitic microstructure and are used in applications requiring high strength and resistance to severe corrosive environments. Due to their superior mechanical properties and corrosion resistance, these steels are increasingly used in engineering applications in oil, gas, petrochemical, offshore, and marine transportation [1, 2]. The vital alloying elements in these steels are Cr, Ni, Mo, and N. The optimal amount of these elements and the appropriate dissolution annealing temperature result in a 50:50 balance between ferrite and austenite, leading to excellent corrosion resistance and mechanical properties [3, 4].

Welding is one of the most important processes in constructing duplex stainless steel structures. Studies show [5] that although super Duplex stainless steels

* *Corresponding Author*
Email: arebrahimi@aut.ac.ir
Address: Department of Materials and Metallurgical Engineering, Amirkabir University of Technology, Tehran, Iran
1. Ph.D. Candidate, 2. Associate Professor

DOI: http://10.22034/IJISSI.2024.2027101.1290
Published by ISSI (Iron & Steel Society of Iran)

(SDSS) show good weldability, these alloys fail due to the increase of ferrite (deviation from phase balance) in the weld zone and the formation of brittle intermetallic phases such as chromium nitride (Cr_2N), chi (Ψ), alpha prime (ά) and especially sigma (σ), cause a significant reduction in corrosion resistance and mechanical properties. Therefore, the accurate selection of welding technique and process parameters is essential to improve phase balance and, thus, corrosion resistance and mechanical properties. The austenite phase is formed during the weld's cooling from the thermal cycle's maximum temperature, with the transformation of the delta ferrite phase to the solid state, which is a function of the cooling rate and chemical composition [6, 7]. Nitrogen is the most important alloying element for forming austenite in welding duplex stainless steels and achieving the re-equilibrium of ferrite/austenite [8, 9]. Since nitrogen is an interstitial element in the austenite and ferrite networks, it can accelerate the formation of austenite in the solid state transformation and improve the phase balance by fast diffusion, especially in ferrite [10]. Considering the crucial role of nitrogen elements in creating phase balance, the loss of nitrogen in the weld pool and the heat-affected zone is one of the critical challenges. Welding with Ar shielding gas led to some nitrogen loss in the weld pool of duplex stainless steel, especially for high-nitrogen types, As reported by Verma et al. [11]; also, shielding gas with small amounts of nitrogen is recommended for TIG, plasma, and MIG welding to obtain weld metal with higher nitrogen levels. Hosseini and Carlson [12] also found that by increasing the number of welding passes or increasing the welding input heat, the amount of nitrogen reduction in the weld pool of two-phase stainless steel increases, and the percentage of ferrite phase in the weld increases significantly and the size of ferrite grains also increases. Also, Westin et al. [13] have reported that the increase of nitrogen gas to Ar shielding gas can compensate for the decrease of nitrogen and facilitate the formation of austenite phase in the weld metal and the heat affected zone (HAZ) in super duplex stainless steel.

TIG welding with active flux (A-TIG) is one of the most promising methods in welding, and it shows a considerable improvement in penetration depth by using a flux layer [14]. The studies conducted by Ramkumar et al. [14] to investigate the effect of three fluxes, NiO, MoO_3, and SiO_2, in active TIG welding of super duplex stainless steel (UNS S32750) with a sheet thickness of 5 mm showed that the use of these fluxes in A-TIG welding caused greater penetration and more excellent depth-to-width ratio. Also, in this research, no significant difference was observed in the different fluxes' microstructure of the welding zone.

The research of Gang et al. [15] in alloying shows that when the amount of cerium in steel is 0%, the impurities are mainly irregular and large, including Al_2O_3 and Al_2O_3-MnS. However, when the amount of cerium in steel is 0.005% or 0.02%, the impurities are primarily spherical and small, including $CeAlO_3$, Ce_2O_2S, and Ce_2O_3. As the amount of cerium increases, the proportion of small-sized impurities gradually increases, the number of impurities per unit area decreases, and the average grain size decreases. In addition, the mechanical properties are improved, and the tensile strength, yield strength, and elongation percentage increase.

The corrosion resistance of duplex stainless steel is due to nanometer-thick passive films on its outer surface [16]. Significant research has been conducted on the semiconducting properties of the passive film in stainless steels, focusing on the effects of pH, electrolyte concentration, and potentiostatic polarization on the density of defects in the passive film [17-20]. Other factors impacting passive film properties, particularly for weld metal, have been studied less. Additionally, most of the research on active TIG welding has concentrated on using flux to achieve maximum penetration depth, but limited studies examining the effect of flux on the microstructure and corrosion behavior of TIG welding on duplex stainless steel.

This research delves into the technical aspects of the active TIG process and its potential for effective alloying in the weld pool. It introduces a new idea that utilizes special fluxes and their regeneration in the weld pool to incorporate elements with minor quantities but significant effects. These elements can significantly optimize the weld pool. This study focuses on one such special flux, cerium oxide flux (CeO_2), and its combined impact with an Ar + 5% N_2 shielding gas mixture in welding 2507 super duplex stainless steel. The effects on microstructure, pitting corrosion behavior, and surface layer characteristics in a 3.5% NaCl aqueous solution are examined.

2. Research Method

The research samples are made of super duplex stainless steel 2507, processed into 6 mm thick plates. The chemical composition of the steel is in Table 1. and complies with the ASTM A240 standard [21]. The chemical composition is balanced to yield approximately equal amounts of ferrite and austenite in solution-annealed conditions. Cerium oxide CeO_2 powder (flux) was also used with 99% purity and 20 μm particle size. Before welding, the surfaces of the samples were sanded and cleaned with acetone. TIG and active TIG welding were performed in a single pass without using filler metal by a TIG welding machine (TECNO JOSH, TIG Weld 300 Ac/Dc) with a 300 Amp model. The machine was equipped with an automatic table to control the welding speed. Ar and a mixed gas of Ar + 5% N_2 with a purity of 99.99% was used for shielding gas. In the active TIG welding process, powder was applied to the sample surfaces. Flux was mixed with acetone and applied to the metal surface using a suitable brush in the desired welding direction.

The flux density was 8-9 mg/cm^2. The samples were then welded according to the specifications in Table 2.

After welding, the weld bead cross-sections from different samples were machined into coupons using wire-cut electrical discharge machining (WEDM). The samples were then prepared, and their microstructure was investigated by electrochemical etching with a solution of 40 g NaOH in 100 g of distilled water at 2v DC for 20 seconds. Subsequently, they were examined with a light microscope (MEIJI model) and a field emission scanning electron microscope (FE-SEM TESCAN-MIRA3 model). The percentage of the ferrite phase was measured using a ferritescope device and image analysis software (AQUINTO). Additionally, grain size measurements were conducted with image analysis software based on the ASTM-E112-96 standard [22].

The sample preparation included sampling from the vertical sections of the welding platform, polishing with up to 1000 grit sandpaper, and washing the samples. All electrochemical tests were conducted using potentiostat instruments (ACM-GillAC & ZIVE SP1 models) with a saturated calomel reference electrode (SCE), platinum auxiliary electrode, and the working electrode (study sample) in a 3.5 wt% sodium chloride solution at room temperature. Before cyclic polarization, electrochemical impedance spectroscopy (EIS), and Mott-Schottky tests, the samples were immersed in the solution as open circuit potential (OCP) for 1 hour to reach a stable potential. Cyclic polarization tests were carried out with a potential sweep rate of 1 mV/s up to a potential of 1500 mVSCE or a corrosion current of 10 mA. Finally, a reverse potential scan assessed the tendency to repassivate. Electrochemical impedance spectroscopy (EIS) tests were conducted in the frequency range from 100 kHz to 10 MHz with a 10 mV amplitude signal. The impedance spectra of each sample were collected, then fitted and analyzed using the EIS analyzer software. Mott-Schottky theory was applied to characterize the electronic properties and density of surface charge carriers as a function of the applied potential. Additionally, the Mott-Schottky test was carried out to investigate the corrosion behavior by analyzing the semi-conductivity property of the oxide film formed on the samples in the potential range of -600 to 1000 mV_{SCE} and a frequency of 1000 Hz.

3. Results and Discussion

3.1. Inspection of welding sections

In Table 3. the specifications of welding processes for different samples are presented. As indicated in Fig. 1. and Table 3. with the conventional TIG welding process and Ar shielding gas (TIG sample), the penetration depth and width of the weld are 2.3 mm and 12.4 mm, respectively. For the welding samples A-TIG CeO_2 (Active TIG welding with cerium oxide flux and Ar shielding gas) and A-TIG CeO_2+5%N_2 (Active TIG welding with cerium oxide flux and Ar + 5% N_2 shielding gas mixture), the depth of welding penetration increased by 9% and 2%, respectively. Additionally, the weld width decreased by 35% and 23%, respectively. Despite the use of the active TIG process, a slight increase in the penetration depth of the weld is observed. However, overall, the weld depth-to-width ratio (D/W) value in samples A-TIG CeO_2 and A-TIG CeO_2+5%N_2 increased by about 42% and 21%, respectively, compared to the TIG sample. Based on Table 3. and research conducted [24], using oxide flux and nitrogen gas raises the welding voltage by increasing the ionization potential. As a result, this leads to higher heat input and greater penetration depth in the weld.

In active TIG welding, active elements on the surface, such as oxygen in steel, cause a higher surface tension in the center of the welded pool. This results in a positive surface tension gradient and heat transfer towards the center, reversing the Marangoni flow [25]. Another important mechanism in increasing the weld penetration depth in the active TIG process is the effect of arc contraction. In the active TIG process, the diameter of the plasma arc column decreases. This reduction in arc size leads to an increase in current density, which increases heat density and ultimately results in deeper penetration of the weld [26]. Therefore, reversing the Marangoni convection and arc contraction are the

Table 1. Chemical composition of super duplex stainless steel 2507.

Symbol	C	Cr	Ni	Mo	N	S	P	Mn	Si	Cu	Fe
Base metal	0.024	25.6	7.12	3.82	0.24	0.006	0.034	0.97	0.297	0.074	Rem.

Table 2. Specifications of welding processes.

Electrode type	EWTH (W2%TH)
welding current	225±2 **A**
Welding speed	2 **mm/s**
Electrode diameter	3.2 **mm**
Angle of the electrode tip	60°
Arc length	2 **mm**
Gas flow rate	16 **l/min**

two main mechanisms that increase the penetration depth in the active TIG welding process. In other words, these factors contribute to an increase in thermal density.

Based on the information from the Ellingham diagram in Table 4. and the standard free energy, we know that cerium oxide is unstable and decomposes when exposed to the arc's heat, releasing oxygen. In addition to standard Gibbs free energy, other factors such as electronegativity, specific electrical resistance, and melting point also increase the ratio of weld depth to width [27-29].

3.2. Microstructural Investigation

Fig. 2(a). displays the microstructure of the base metal (BM) of the 2507 alloy. It depicts a balanced microstructure with austenite islands in a large ferrite matrix. Table 5. provides the quantitative values of austenite and ferrite phases in the BM and weld samples, as measured by a ferrite scope device. Additionally, Fig. 2(b). illustrates the volume percentages of ferrite (in yellow) and austenite (in red) phases in the BM, as determined by image analysis software. These results align with those obtained using the ferrite scope device. The grain sizes of ferrite and austenite in the BM are approximately 15.5 µm and 21.7 µm, respectively.

In Fig. 2(c). the microstructure of the TIG sample shows a non-equilibrium combination of the ferrite phase as the matrix and the austenite phase. The austenite phases include narrow grain boundary austenite grown at the ferrite grain boundary, wedge-shaped Widmanstätten austenite, fine intragranular austenite, and other precipitation inside the ferrite grains. Additionally, fine and dense intragranular austenites in some areas of the microstructure suggest the presence of secondary austenites. It is important to note that grain boundary austenite and Widmanstätten lateral plates are formed at higher temperatures. In comparison, intragranular austenite particles require more driving force and are deposited later at lower temperatures. Similar observations were also reported by Ramkumar and Muthupandi et al. [14, 33].

Table 3. Specifications of welding samples.

Sample name	Welding process	Flux	Shielding gas	Weld width، W mm	Welding penetration depth، D, mm	Depth to width ratio of the weld, D/W	Voltage V	Heat input KJ/mm
TIG	TIG	-	Ar	12.4	2.3	0.19	12.5	1.41
A-TIG CeO_2	A-TIG	CeO_2	Ar	9.2	2.5	0.27	14	1.58
A-TIG CeO_2+5%N_2	A-TIG	CeO_2	Ar + 5%N_2	10.1	2.35	0.23	14.8	1.63

Fig. 1. Macrograph of welding samples (a) TIG (with Ar gas) (b) A-TIG CeO_2 (c) A-TIG CeO_2+5% N_2.

Table 4. Physical and chemical properties of used fluxes [30-32].

Flux	Gibbs free energy ΔG°(KJ/mol.k)	melting point (ºC)	Atomic radius (pm)	Specific electrical resistance (Ωm)	electronegativity (Relative scale to H)
CeO_2	-785	2400	Ce=181.8	3	Ce=1.12

Table 5. Ferrite and austenite contents.

Sample Name	Austenite Phase %	Ferrite Phase %
BM	50.5	49.5
TIG	42.1	57.9
A-TIG CeO_2	49.1	50.9
A-TIG CeO_2+5% N_2	67.4	32.6

The narrowness and fineness of the austenite phase, along with a significant decrease in austenite content (42.1%) in the TIG sample compared to the base metal, are depicted in Fig. 2(c). and Table 5. This phenomenon is linked to the partial transformation of ferrite to austenite in the solid state, involving the nucleation and growth of austenite, as well as the cooling rate and the amount of nitrogen in the weld pool [5]. Table 6. illustrates a significant decrease in nitrogen in the weld metal in the TIG sample. This decrease suggests the release of nitrogen in the weld pool [33], which is a highly influential factor in forming the austenite phase and, consequently, in reducing the austenite content.

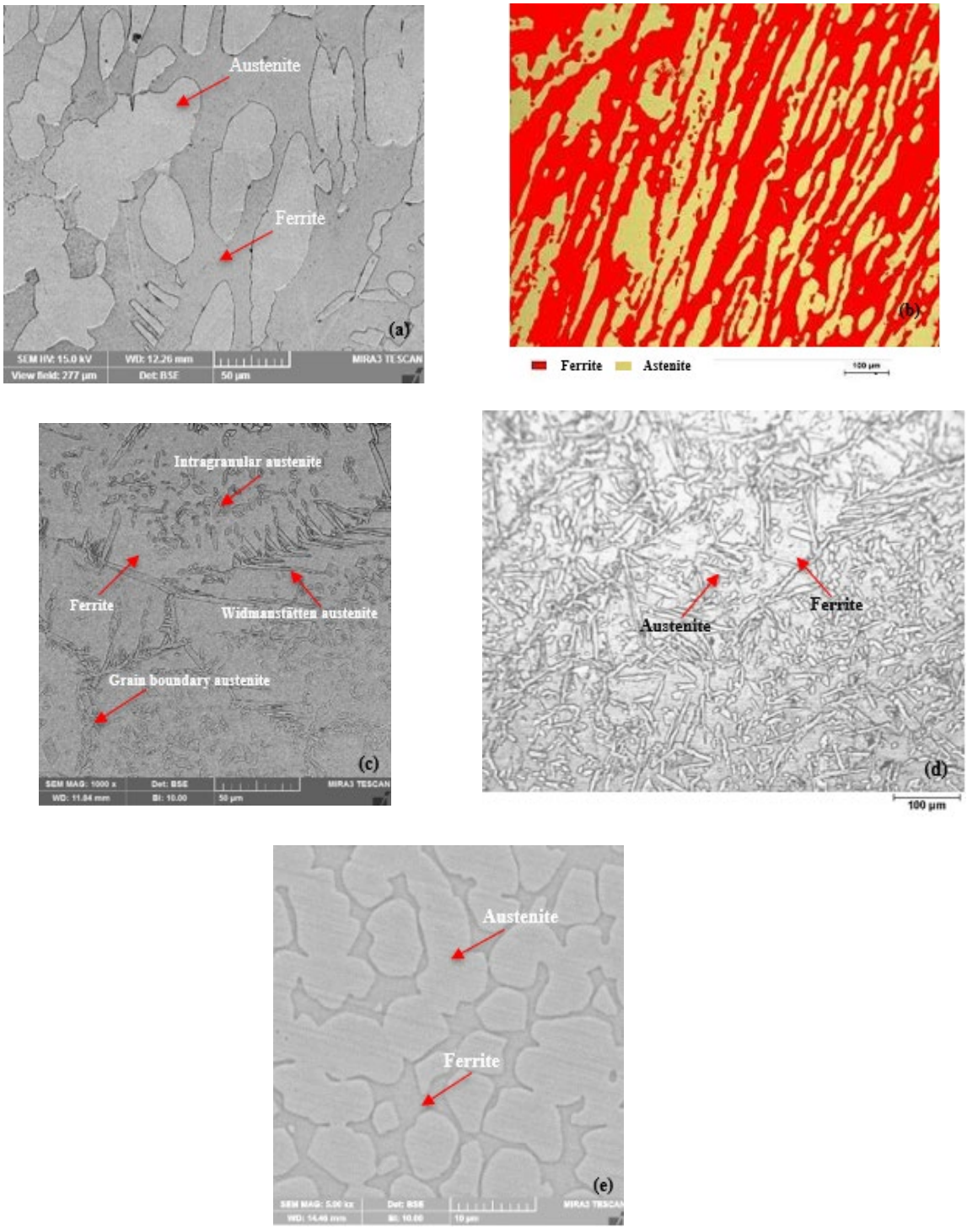

Fig. 2. Microstructure images, (a) BM sample, (b) BM sample with image analysis software, (c) TIG sample, (d) A-TIG CeO_2 sample, and (e) A-TIG CeO_2+5%N_2 sample.

The microstructure of the A-TIG CeO_2 sample, as shown in Fig. 2(d). indicates that the sharp and rough angles of the austenite phases are reduced. Additionally, the size of the ferrite and austenite grains is decreased in this sample compared to the BM and TIG samples. According to Table 5. the phase balance in this sample is in good agreement with the BM sample, as the amount of austenite is 49.1%. This improved phase balance is attributed to features of the active TIG welding process and the presence of cerium element in the welding pool. The increase in thermal density in the active TIG process [27] affects the cooling rate of the weld pool, allowing more austenites to form and grow. Furthermore, the cerium oxide flux adds cerium element to the weld pool after reduction. Although this amount is small, cerium element is an austenite-stabilizing element. It has been reported that higher concentrations of surface active elements such as sulfur and oxygen have a beneficial effect on keeping nitrogen and preventing its release in the welding pool. As seen in Table 6. the active TIG process in the A-TIG CeO_2 sample retains more nitrogen in the weld pool, which helps increase the austenite phase and approach the 50:50 phase balance.

The microstructure of the A-TIG CeO_2+5%N_2 sample, shown in Fig. 2(e). reveals a combination of the ferrite phase as the matrix and the austenite phase. Notably, there is an absence of Widmanstätten austenite phases and austenite with blade and needle shapes in this sample. An increase in the austenite with spherical and quasi-spherical shapes is evident, making the microstructure closely resemble the equilibrium microstructure of BM. Overall, there is a significant increase in the austenite phase. Furthermore, there is a noteworthy decrease in the grain size of both ferrite and austenite phases compared to BM and TIG samples. The size of ferrite and austenite grains is approximately 3.8 and 4.9 micrometers, respectively. As the grain boundaries are favorable places for the nucleation and growth of austenite [5], reducing the grain size increases the austenite phase effectively. The grain size of both ferrite and austenite phases is about four times smaller than that of BM.

On the other hand, the phase balance in duplex stainless steel is very dependent on diffusion, and nitrogen, as a solid austenite-stabilizing element, is in the atomic network in the form of tiny interstitial atoms with a high diffusion rate, which is the critical factor for controlling the phase balance under the conditions of welding cooling [5]. According to the research [35], nitrogen absorption in the welding pool is much higher than the predicted values in equilibrium conditions. This issue is attributed to monoatomic nitrogen in the electric arc plasma, which is formed due to the partial dissociation of diatomic nitrogen. The significant increase of nitrogen in the sample A-TIG CeO_2+5%N_2, in Table 6. is evident; Therefore, the presence of 5% nitrogen gas in the shielding gas can increase the amount of nitrogen in the weld pool and compensate for the nitrogen released from the weld pool during welding and increase the austenite phase; As a result, the combined use of cerium oxide flux and nitrogen gas and the features of the active TIG process can be considered as the cause of this morphology.

Table 6. shows the values of effective elements in pitting corrosion in SEM-EDS analyses performed on welding samples.

$$PREN = wt\%\ Cr + 3.3(wt\%\ Mo + 0.5 \times wt\%\ W) + 30 \times wt\%\ N \quad [36] \qquad \text{Eq.(1)}$$

The pitting corrosion resistance numbers were calculated based on Eq.(1). The TIG sample had the lowest value, 48, while the A-TIG CeO_2+5%N_2 sample had the highest value, 54.1.

As shown in Fig. 3(a) and 3(b). the inclusions in the TIG sample are mostly elongated and often large, and their distribution is irregular. The presence of cerium element in the A-TIG CeO_2 and A-TIG CeO_2+5%N_2 welding samples in Fig. 3(c) and 3(d). has caused changes in the size, shape, and distribution of inclusions. The inclusions are minor, spherical, and have a more uniform distribution, consistent with other research conducted [15, 37-40] to investigate the effect of cerium element in steelmaking. The SEM-EDS analysis of one of the inclusions in the A-TIG CeO_2+5%N_2 sample is recorded in Table 7.which shows the presence of some cerium element in the inclusion composition.

The SEM-EDS spot analysis results of austenite and ferrite phases in the base metal are presented in Table 7. Upon examining the elemental composition of the austenite and ferrite phases, it is evident that austenite-stabilizing elements such as nickel and nitrogen are more abundant in the austenite phase than in the ferrite phase. Conversely, the ferrite phase exhibits higher levels of ferrite-stabilizing elements, such as chromium and molybdenum, than the austenite phase. These findings confirm the presence of a separation phenomenon in these steels. Additionally, SEM-EDS-MAP analysis was

Table 6. SEM-EDS analysis of welding samples.

Sample Name	%Cr	%Mo	%N	PREN	%Others
TIG	26,96	4.93	0.16	48.03	Bal
A-TIG CeO_2	26.01	4.81	0.28	50.28	Bal
A-TIG CeO_2+5%N_2	27.28	5.02	0.34	54.05	Bal

conducted to detect the presence of cerium in the weld pool of a weld sample using cerium oxide flux and Ar + 5% N_2 gas, as illustrated in Fig. 4. The chemical analysis of the weld pool indicates the presence of scattered cerium elements.

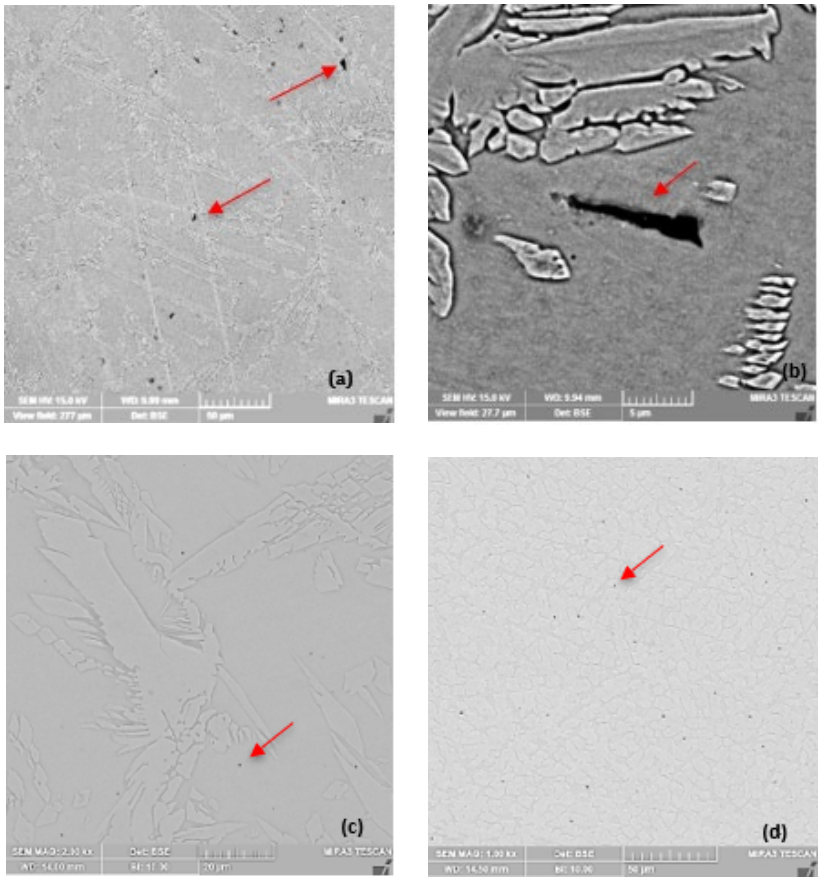

Fig. 3. Pictures of the state of inclusions in (a, b) TIG sample, (c) A-TIG CeO_2 sample, and (d) A-TIG CeO_2+5%N_2 sample.

Table 7. SEM-EDS analysis.

Sample name	%Cr	%Ni	%N	%Mo	%Others
Austenite phase in BM	26.95	4.2	0.71	4.8	Bal.
Ferrite phase in BM	28.6	2.4	0.33	6.1	Bal.
Impurities in A-TIG CeO_2+5%N_2 sample	8.01	0.66	-	2.06	Si 33.8, Ce 0.36, Bal.

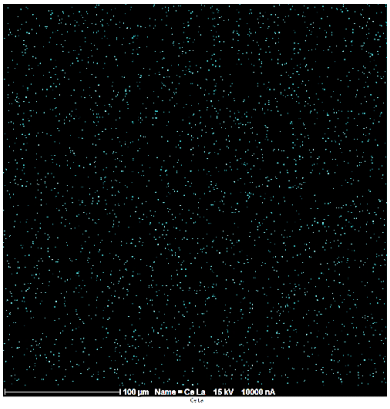

Fig. 4. SEM-EDS-MAP analysis to identify A-TIG CeO_2+5%N_2 sample.

3.3. Analysis of Pitting Corrosion

In order to study pitting corrosion behavior accurately, the samples were immersed in a 3.5% sodium chloride solution for 1 hour. Afterward, these were subjected to a cyclic polarization test in the same solution to compare and analyze their behavior. The diagram in Fig. 5. shows the results of the cyclic polarization test for both the welding samples and the base metal (BM) of 2507 super duplex stainless steel. Additionally, the recorded data from fitting these curves include corrosion potential (E_{corr}), pitting potential (E_{pit}), protection or repassivation potential (E_{rp}), passivation potential range (E_{pit}-E_{corr}), corrosion current density (I_{corr}) and corrosion current density (I_{pass}), which are documented in Table 8.

Based on Fig. 5. and Table 8. all samples exhibit similar active-passive behavior. The BM curve displays some scatter in the corrosion current density range from the corrosion potential Ecorr to a potential of +500 mV vs. SCE, indicating the formation of unstable pits. This dispersion is likely influenced by the electrochemical interaction between the austenite and ferrite phases, as well as the characteristics of the surface protective film [41]. The corrosion potential of the BM is -140 mV vs. SCE, while the corrosion potential of the TIG sample is -203 mV vs. SCE. The BM potential is nobler than the TIG sample, suggesting a greater tendency to corrosion in the TIG sample, although it does not necessarily represent the actual corrosion kinetics. E_{pit} and E_{rp} in the TIG sample have been significantly reduced compared to the BM. A lower Epit indicates less resistance to the formation of stable pits, and a lower protection potential (E_{rp}) indicates weaker resistance to pit growth and a reduced tendency to passivate again [42]. The TIG sample exhibits the lowest corrosion, pitting, and protection potential values. It has the highest corrosion current density and passivity values, significantly differing from other samples. In other words, the TIG sample demonstrates the weakest electrochemical behavior compared to another sample.

According to Fig. 5. and Table 8. the A-TIG CeO_2 and A-TIG CeO_2+5%N_2 samples have shown significant increases in corrosion, pitting, and protection potentials compared to the TIG sample. Additionally, the corrosion current density and passivity current density have been reduced and improved by about 22 times. The pit growth rate in these welding samples has decreased compared to the TIG sample, and the potential for initiating stable pits (Epit and Erp) has also increased. Overall, the resistance to pitting corrosion in the A-TIG CeO_2 sample, especially in the A-TIG CeO_2+5%N_2 sample, has significantly improved compared to the TIG sample. The research conducted [38] suggests improving the resistance to pitting corrosion in steelmaking. It has also been reported that the cerium element reduces the micro-grooves between the matrix and the inclusions, where pitting corrosion may initiate.

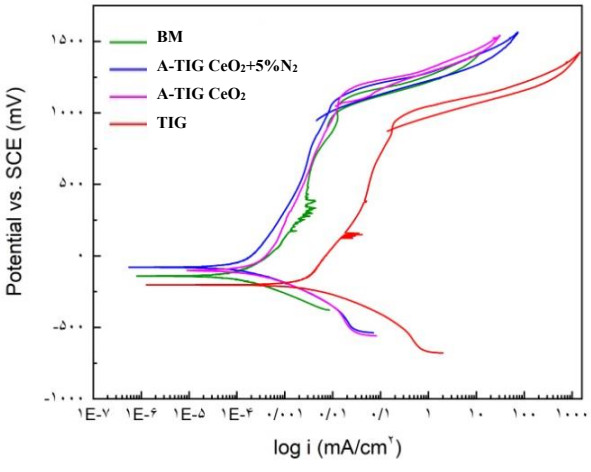

Fig. 5. Comparison of cyclic polarization diagrams of BM, TIG, A-TIG CeO_2, and A-TIG CeO_2+5%N_2 samples.

Table 8. Data extracted from cyclic polarization tests.

Sample Name	E_{corr} (mV vs. SCE)	E_{pit} (mV vs. SCE)	E_{pit} - E_{corr} (mV vs. SCE)	E_{rp} (mV)	I_{corr} (µA/cm²)	I_{pass} (µA/cm²)
BM	-140	1039	1179	1004	0.101	2.91
TIG	-203	919	1122	887	2.531	63.28
A-TIG CeO_2	-101	1089	1190	1054	0.201	3.36
A-TIG CeO_2+5%N_2	-80	1061	1141	999	0.116	2.85

The electrochemical behavior of the welding samples with cerium oxide flux is very close to the BM sample, and even in some parameters, a better behavior is observed than the BM sample, which has a direct relationship with the stability of their surface protective film, which will be discussed further. Also, since the formation of various precipitations and secondary phases in the welding process have a destructive effect on the pitting resistance, based on the research [43], the addition of N and Ce elements as alloying elements effectively prevents the formation of the sigma phase. According to another study [44], adding cerium reduces the sigma phase formation and increases corrosion resistance significantly. The sigma phase dramatically reduces the surface layer's uniformity, stability, and protection [45]. It has also been reported that cerium in solid solution purifies grain boundaries and refines grains in steel. So, a small amount of homogenously distributed cerium in duplex stainless steels delays the formation of secondary phases [43] and significantly reduces the formation of the σ phase [44]. Some researchers [46] have suggested that when the atomic size difference of elements is more than 8%, it prevents the formation of the sigma phase. Therefore, large Ce atoms in this research are expected to delay the sigma phase formation because the atomic radius difference between Fe-Cr-Mo and Ce is more than 20%. Therefore, based on the studies of other researchers, the microstructural investigations, and the results of the corrosion tests conducted in this research, a significant reduction of precipitation and destructive secondary phases, such as the sigma phase in welding samples with cerium oxide flux, is expected. In general, the improvement of the pitting corrosion behavior of these samples can be attributed to the presence of the cerium element in the weld pool in the A-TIG CeO_2 sample and the combined presence of nitrogen gas and the cerium element in the A-TIG CeO_2+5%N_2 sample; Its effects on microstructure, grain size, inclusions, phase balance, and protective film are evident.

3.4. Analysis of Electrochemical Impedance Spectroscopy (EIS) Tests

In this research, an electrochemical impedance spectroscopy test was utilized to investigate how adding cerium and nitrogen elements impacts the corrosion resistance of passive films and to conduct a more detailed study of the metal/solution interface. The findings are presented in Fig. 6.

According to Fig. 7. the impedance response and data interpretation were carried out using the electrical equivalent circuit $R_s(CPE_1R_1)(CPE_2R_2)$ to fit the impedance spectrum of the samples. In this circuit, the passive film was characterized by CPE1, representing the capacitance of the passive film coupled with the resistance R_1. CPE_2 represents the double-layer capacitance, R_2 represents the charge transfer resistance, and R_s represents the resistance of the solution. The constant phase element CPE describes the non-ideal capacitance in the circuit, replacing the pure capacitance component C due to surface heterogeneity [23, 47, 48]. Figs. 6 and 7. demonstrate that all samples conform to this equivalent circuit, suggesting a similar corrosion mechanism for all samples.

Fig. 6(a). reveals that all the spectra are characterized as unfinished semi-arcs in the Nyquist plots, indicating a similar passive mechanism on the samples [49]. The radius of the capacitive semi-arcs of the samples is associated with the resistance of the passive film [23]. As seen in Fig. 7. the TIG sample shows the lowest capacitive arc, or in other words, the lowest resistance and surface protection by the passive film. In the A-TIG CeO_2 sample, the resistance of the passive film increases, and using the shielding gas Ar + 5% N_2 mixture in the A-TIG CeO_2+5%N_2 sample increases the resistance of the passive film. Therefore, the effect of cerium and nitrogen elements in the welding pool on improving the surface passive film is quite evident.

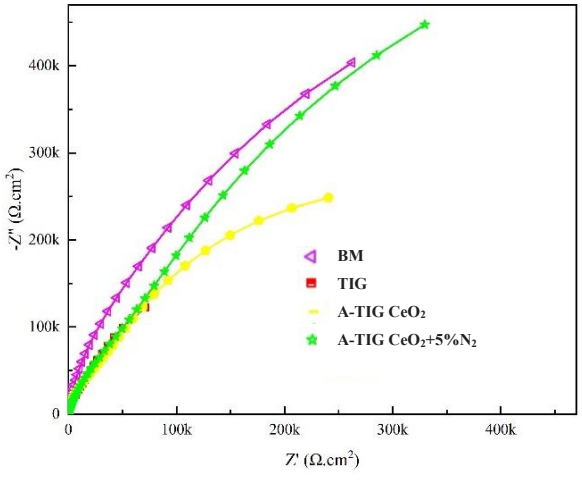

Fig. 6. Nyquist plots of BM, TIG, A-TIG CeO_2, and A-TIG CeO_2+5%N_2 samples.

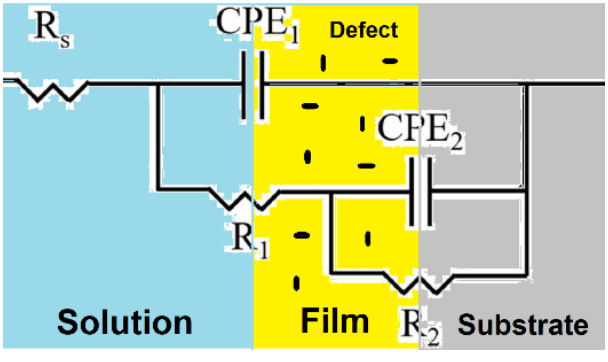

Fig. 7. Electrical Equivalent Circuit (EEC) to interpret the results.

Table 9. lists the parameters fitted using the electrical equivalent circuit. It has been reported [23, 47] that Rp represents the polarization resistance ($R_p = R_1 + R_2$), where R_1 and R_2 are parameters obtained from the fitting results and generally correspond to the charge transfer resistance at the film/electrolyte interface. An increase in R_p indicates that charge transfer has become more difficult, leading to improved corrosion resistance. Therefore, R_p is an essential parameter for evaluating anti-corrosion properties.

The A-TIG CeO_2+5%N_2 and BM samples showed the highest resistance (R_p), with a slight difference, followed by the A-TIG CeO_2 sample. Finally, the TIG sample exhibited the lowest resistance by a significant difference. The A-TIG CeO_2+5%N_2 sample had the maximum amount of R_1 and the minimum value of CPE_1 compared to the other samples, which suggests that its passive film has optimal resistance to corrosion due to having the fewest defects [48, 49]. Additionally, the BM and A-TIG CeO_2+5%N_2 samples demonstrated the highest value of R_2, indicating that the film on them has the highest resistance against charge transfer processes at the base metal/solution interface. Conversely, the protective film of the TIG sample possesses the worst protective properties. Therefore, the A-TIG CeO_2+5%N_2 sample exhibits the best corrosion resistance. The results obtained from impedance tests were also confirmed with cyclic polarization curves.

The grain size has significantly decreased, especially in the A-TIG CeO_2+5%N_2 sample. According to research [15, 37-40], reducing grain size in the austenite and ferrite phases increases the grain boundaries, providing more suitable locations for creating oxide films. It has been noted that oxide film formation begins at high-energy sites like grain boundaries; hence, reducing grain size accelerates the kinetics of oxide film formation. Additionally, as the structure becomes smaller and more homogenized, the oxide film formed on the duplex stainless steel exhibits a more significant correlation with the background, enhancing corrosion resistance.

3.5. Analysis of Mott-Schottky Tests

Fig. 8. illustrates the Mott-Schottky plot of $1/C^2$ as a function of applied potential, which was utilized to analyze the semiconductor properties of the samples under study.

The Mott-Schottky theory is founded on a depletion region within the passive film, which forms a space charge capacity (C). Eqs.2 and 3 describe the relationship between the space charge capacity and the applied potential (E) for a semiconductor junction. These equations are also utilized to determine the presence of donors and acceptors [23, 47, 48].

$$\frac{1}{C^2} = -\frac{2}{\varepsilon\varepsilon_0 e N_D}\left(E - E_{FB} - \frac{kT}{e}\right) \quad \text{n- type} \quad \text{Eq.(2)}$$

$$\frac{1}{C^2} = -\frac{2}{\varepsilon\varepsilon_0 e N_A}\left(E - E_{FB} - \frac{kT}{e}\right) \quad \text{p- type} \quad \text{Eq.(3)}$$

Table 9. The fitting parameters for the impedance spectra of samples.

Sample Name	R_1 (ohm.cm^2)	R_2 (ohm.cm^2)	CPE_1 (Fs^{n-1}.cm^{-2})	CPE_2 (Fs^{n-1}.cm^{-2})
BM	52328	1.18× (10^6)	5.15× (10^{-5})	1.85× (10^{-5})
TIG	9746	2.48× (10^5)	9.98× (10^{-5})	9.82× (10^{-5})
A-TIG CeO_2	31899	5.82× (10^5)	3.43× (10^{-5})	3.05× (10^{-5})
A-TIG CeO_2+5%N_2	48159	1.21× (10^6)	3.17× (10^{-5})	2.38× (10^{-5})

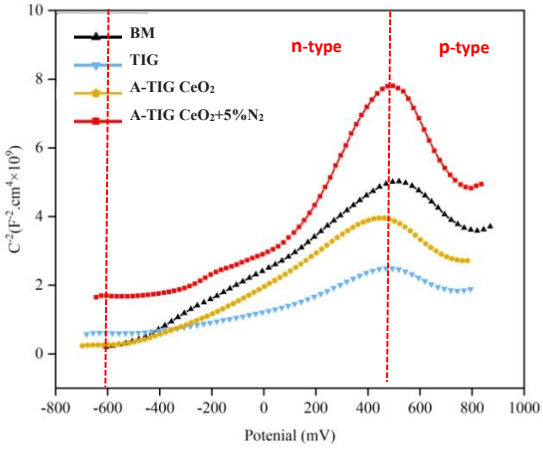

Fig. 8. Comparison of Mott-Schottky plots of the BM, TIG, A-TIG CeO_2 and A-TIG CeO_2+5%N_2 samples.

Where N_A and N_D represent the acceptor and donor concentration, respectively, e is the electron charge (1.6 x 10^{-19}C), T is the absolute temperature (K), ε_0 is the vacuum permittivity (8.854×10^{-14} F/cm), ε represents the dielectric constant (15.6 for stainless steel), k is the Boltzmann constant (1.38×10^{-23} J/K), EFB refers to flat band potential (vs. SCE), and E applied potential (vs. SCE).

Based on Fig. 8. the Mott-Schottky plots exhibit a similar trend for all samples, divided into two parts. In region 1, with a potential range from about -600 to 480 mV and a positive graph slope, the passive film mainly comprises Fe_2O_3 [23], showing n-type semiconductor behavior due to increased anionic vacancies [50]. In region 2, with a potential range from about 480 to 750 mV and a negative slope, the graph exhibits p-type semiconductor behavior, likely due to increased cation vacancies [52]. The charge carrier characteristic in the oxide film changes from n-type to p-type as we move from region 1 to region 2. In the case of duplex stainless steel, the passive films display p-type and n-type characteristics, corresponding to the inner and outer layers of the oxide layer, respectively [50]. The impedance tests confirmed the presence of two inner and outer oxide layers for super duplex stainless steel 2507, as indicated by the selected equivalent circuit.

According to data extracted from Mott-Schottky tests in Table 10. and Zhang et al.'s research [23], the curve slope of the A-TIG CeO_2+5%N_2 sample has increased significantly compared to other welding samples and even compared to the BM in all areas, which indicates the drop of donor and acceptor, or in other words, a decrease in the density of point defects in the protective film. This shows that the samples welded with cerium oxide flux, especially with nitrogen gas mixture, have a greater tendency to form a dense chromium oxide protective film. Also, based on the research conducted by Sahli et al. [53] and the data in Table 10. the lower amount of N_D indicates a lower rate of dissolution of cations at the surface/solution layer interface. It is also reported that adding Ce to the alloy has valuable effects on inclusions and corrosion resistance. First, it reduces the interface between the inclusion and the background, which act as defect sites in the protective film and corrosion initiation sites. Second, adding Ce to the alloy leads to stable inclusions containing Ce with a low amount of chromium and increased chromium oxide and hydroxide in the surface film. This improves the corrosion resistance, so adding Ce to the duplex stainless steel alloy enhances the stability of the surface film [15,37,38,40,54]. Therefore, adding small amounts of cerium to the super duplex stainless steel 2507 weld pool achieves better chemical stability for the passive film. Also, according to the cyclic polarization tests, in the welding samples with cerium oxide flux, the increase in pitting potential with the addition of cerium can be attributed to the decrease in the diffusion of cation vacancies and the increase in the destruction rate of cation vacancies.

It has been reported [55] that a lower flat band potential (E_{fb}) results in a lower reactivity of the protective oxide layer with dissolved anions. Referring to Table 10. the tendency of the oxide film to react with dissolved anions is similar to that of the BM for the welding samples with cerium oxide flux. In contrast, the TIG sample exhibits a significantly greater reactivity.

The main defects in n-type semiconductors are oxygen vacancies, suitable places for absorbing aggressive ions, including chloride ions. Therefore, increasing the density of defects increases the probability of absorbing the attacking ion and destroying the protective oxide film. According to the relation $d=\frac{\varepsilon\varepsilon_0 A}{C}$, if the capacitance is equal to C, the amounts of 15.6 and 8.85×10^{-12} Farad/m are considered for ε and ε_0, respectively [23]. It is possible to calculate the process of changes in the thickness of the oxide film with increasing potential. Fig. 9. displays the calculated changes in passive film thickness relative to the potential for the studied samples. The thickness of the passive film increases with potential up to approximately 480 mV. Notably, the A-TIG CeO_2+5%N_2 sample exhibits a significant increase in passive film thickness compared to other samples. Additionally, the growth rate of the oxide film in the A-TIG CeO_2+5%N_2 sample is non-uniform, with a slope that differs from other samples whose trend remains consistent within the studied range. According to the research of Wang et al. [55], this non-uniformity in the A-TIG CeO_2+5%N_2 sample is attributed to its lower density of defects, resulting in less dissolution of the protective oxide film.

Table 10. Data extracted from Mott-Schottky tests.

Sample Name	Flat band potential (mV)	Zone 1		Zone 2	
		$\times10^{20}$, N_D (cm^{-3})	slope	$\times10^{20}$, N_A (cm^{-3})	slope
BM	-509.3	15.18	5.94	15.98	-5.64
TIG	-272.2	27.05	3.34	27.59	-3.27
A-TIG CeO_2	-485.1	18.39	4.91	16.09	-5.61
A-TIG CeO_2+5%N_2	-498.93	7.2	12.56	6.77	-13.35

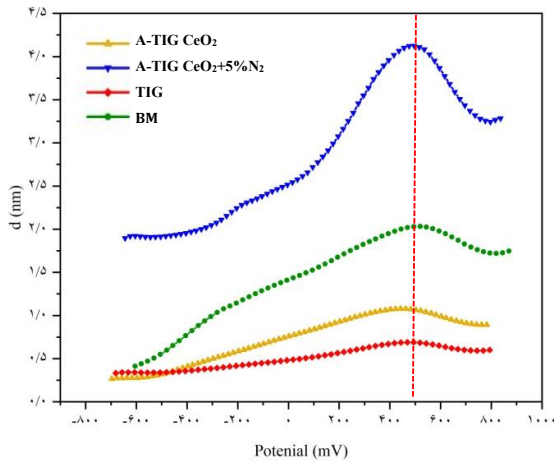

Fig. 9. Changes in oxide film thickness with increasing potential for the BM, TIG, A-TIG CeO_2, and A-TIG CeO_2+5%N_2 samples.

4. Conclusions

Based on the investigations carried out in this research, the following results can be stated:

- In the TIG sample, the phase balance concerning the base metal was disturbed, and the austenite phase decreased to 42.1%. In the A-TIG CeO_2 sample, there was an increase in the formation of the austenite phase, reaching a value of 49.1%, which aligns with the phase balance in the base metal sample.
- The microstructure of the A-TIG CeO_2+5%N_2 sample does not contain Widmanstätten austenite. Instead, there is a significant increase in the presence of austenite with spherical and quasi-spherical shapes, making its morphology very similar to BM. The grain size of both ferrite and austenite phases is about four times smaller than that of BM.
- The inclusions in the TIG sample are mainly elongated, irregularly distributed, and often large. However, the inclusion of the cerium element in the A-TIG CeO_2 and A-TIG CeO_2+5%N_2 samples has resulted in minor, spherical, and more uniformly distributed inclusions.
- The electrochemical behavior in active TIG welding samples, particularly in the A-TIG CeO_2+5%N_2 sample, has significantly improved compared to the TIG sample. In particular, the corrosion current density and the passive current density have decreased by about 22 times and show the closest pitting corrosion resistance compared to BM, and even better behavior than BM was observed in some parameters. This issue is a promising sign of the valuable effect of cerium element in the welding pool and the presence of cerium and nitrogen twins in the welding pool.
- The resistance of the passive film increases significantly in the A-TIG CeO_2 sample. Additionally, in the A-TIG CeO_2+5%N_2 sample, the significant reduction in grain size leads to the lowest defects and the highest resistance to charge transfer processes in the passive film. This indicates the highest increase in corrosion resistance compared to other samples. Therefore, the effect of cerium and nitrogen elements in the welding pool on improving the surface passive film is evident.
- The results of Mott-Schottky tests suggest a promising future for using flux-containing cerium in welding. Particularly, when combined with an Ar + 5% N_2 shielding gas mixture, the samples tend to form a dense protective film with increased chemical stability. This potential for future applications underscores the significance of our findings.

List of symptoms

D: Weld depth
W: Weld width
Ar: Argon gas
N_2: Nitrogen gas
E_{corr}: Corrosion potential
E_{pit}: Pitting potential
E_{rp}: protection or repassivation potential
E_{pit}-E_{corr}: Difference between pitting potential and corrosion potential
I_{corr}: Corrosion current density
I_{pass}: Passivity current density
C: Space load capacity
R_s: Solution resistance
R_1: Resistance of the passive film
R_2: Charge transfer resistance
$CPE_{1,2}$: Dielectric properties of the inner and outer oxide film
Rp: Polarization resistance
NA, ND: Donor, and acceptor
e: Electron charge
T: Temperature K
K: Boltermann's constant
EFB: Flat band potential
E: Applied potential
Ψ: Phase of tea

ά: Phase of alpha prime
σ: Sigma phase
ε_0: Vacuum permeability coefficient
ε: Dielectric constant for stainless steel

References

[1] Nilsson J.O, Chai G, The physical metallurgy of duplex stainless steels, In: Proceedings of the Duplex Stainless Steel Conference, Beaune, France. 2010.
[2] Deng B, Jiang Y, Gong J, Zhong C, Gao J, Li J, Critical pitting and repassivation temperature for duplex stainless steel in chloride solutions, Electrochim Acta. 2007.
[3] Deng B, Jiang Y.M, Gao J, Li J, Effect of annealing treatment on microstructure evolution and the associated corrosion behavior of a super-duplex stainless steel, J Alloys Compd. 2010; 493(1): 461-4.
[4] Tan H, Jiang Y, Deng B, Sun T, Xu J, Li J, Effect of annealing temperature on the pitting corrosion resistance of super duplex stainless steel UNS S32750, Mater Charact. 2009; 60(9): 1049-54.
[5] Lippold J.C, Kotecki D.J, Welding Metallurgy and Weldability of Stainless Steel, John Wiley & Sons; 2005: 230-62.
[6] Chen T.H, Yang J.R, Microstructural characterization of simulated heat-affected zone in a nitrogen-containing 2205 duplex stainless steel, Mater Sci Eng. 2002; A338(1): 166-81.
[7] Nowacki J, Łukojc A, Microstructural transformations of heat-affected zones in duplex steel welded joints, Mater Charact. 2006; 56(4): 436-41.
[8] Hänninen H.J.R, Ilola R, Tervo J, Laitinen A, Effects of processing and manufacturing of high nitrogen-containing stainless steels on their mechanical, corrosion, and wear properties, J Mater Process Technol. 2001; 117(3): 424-30.
[9] Li J, Xiao X, Zhao J, Jiang L, On the behavior of nitrogen in a low-Ni high-Mn super duplex stainless steel, Mater Des. 2011; 32(4): 2199-205.
[10] Charles J, Duplex stainless steels a review after DSS'07 held in Grado, Steel Res Int. 2008; 79(6): 455-65.
[11] Verma J.R.T, Effect of welding processes and conditions on the microstructure, mechanical properties, and corrosion resistance of duplex stainless steel weldments, Manufacturing Processes. 2017; 25: 134-52.
[12] Hosseini V.A, Hurtig K, Karlsson L, Nitrogen loss and effects on microstructure in multipass TIG welding of a super duplex stainless steel, Mater Des. 2016; 98: 88-97.
[13] Westin E.M, Bylund Å.L, Pettersson R.A, Effect on microstructure and properties of super duplex stainless steel welds when using backing gas containing nitrogen and hydrogen, Weld World. 2014; 58: 347-54.
[14] Ramkumar K.D, Radhakrishna V,S, Tiwari A, Anirudh S. Studies on the structure-property relationships and corrosion behavior of the activated flux TIG welding of UNS S32750, Manufacturing Processes. 2016.
[15] Gong W, et al. Effects of Ce on microstructure and mechanical properties of LDX2101 duplex stainless steel, Metals. 2020; 10.
[16] Zhang X, Luo H.F, Zhou T, Zhao Y.L, Ling Z, Corrosion resistances of metallic materials in environments containing chloride ions: A review, Trans Nonferrous Met Soc China. 2022; 32: 377-410.
[17] Fattah-Alhosseini A, Shirsat A.B, Electrochemical behavior assessment of Alloy 22 (UNS N16122) in hydrochloric acid solutions by electrochemical impedance spectroscopy and Mott–Schottky analyses, Anal Bioanal Electrochem. 2015; 7: 728-38.
[18] Tsuchiya S, Semiconductor properties and protective role of passive films of iron base alloys. Corros Sci. 2017; 49: 195-212.
[19] Carmezim M, Montemor M, Belo M.D.C, Capacitance behavior of passive films on ferritic and austenitic stainless steel, Corros Sci. 2015; 47: 581-91.
[20] Fattah-Alhosseini A, Ghoranneviss M, Saatchi A, Raeissi K, Effect of solution concentration on semiconducting properties of passive films formed on austenitic stainless steels. Corros Sci. 2011; 52: 215-9.
[21] American Society for Testing and Materials, Standard specification for chromium and chromium-nickel stainless steel plate, sheet, and strip for pressure vessels and for general applications, ASTM International; 2018.
[22] American Society for Testing and Materials, Standard Test Methods for Determining Average Grain Size. ASTM-E112, 96 (Reapproved 2004).
[23] Zhang J, Hu X, Chou K, Effects of Ti addition on microstructure and the associated corrosion behavior of a 22Cr-5Ni duplex stainless steel, Mater Corros. 2021; 72(7): 1201-14.
[24] Lancaster J, The physics of welding, Pergamon Press; 1986.
[25] Mills K.C, Brooks R.F, Shirali A, Marangoni effects in welding, Philos Trans R Soc A Math Phys Eng Sci. 1998; 356: 911-25.
[26] Berthier A, Poupard P, Carin M, Valensi F, Pellerin S, TIG and A-TIG welding experimental investigations and comparison to simulation: Part 1: Identification of Marangoni effect, Sci Technol Weld Join. 2012; 17: 609-15.
[27] Chen K.T, Lin K.L, Comparison between TiO_2- and SiO2-flux assisted TIG welding processes, J Nanoscience Nanotechnol. 2012; 12(8): 6359-67.
[28] Lowke J, Tanaka M, Ushio M, Mechanisms giving increased weld depth due to a flux, J Phys D Appl Phys. 2005; 38(18): 3438.
[29] Lin K.T, Peng Y, UNS S31603 stainless steel tungsten inert gas welds made with microparticle and nanoparticle oxides, Materials. 2014; 7: 4755-72.
[30] Chakravarthy S.J, Parameswaran P, Flux

bounded tungsten inert gas welding for enhanced weld performance—A review, J Manuf Processes. 2017; 28: 116-13.
[31] Conder K, Electronic and ionic conductivity in metal oxides. Paul Scherrer Institute; 2012.
[32] Gaskell D.R, Introduction to thermodynamics of materials. 3rd ed.
[33] Muthupandi V, Srinivasan P.B, Seshadri S.K, Sundaresan S, Effect of weld metal chemistry and heat input on the structure and properties of duplex stainless steel welds, Mater Sci Eng. 2003; 358:9-16.
[34] Hosseini V, Karlsson L, Physical and kinetic simulation of nitrogen loss in high-temperature heat-affected zone of duplex stainless steels, Materialia. 2019; 6: 100325.
[35] De Toit M, The behaviour of nitrogen during the autogenous arc welding of stainless steel. Department of Materials Science and Metallurgical Engineering, University of Pretoria; 2001.
[36] Han Y, Zhao Y, Jing H, Gao Z, Xu L, Zhang Z, Zhao L, Microstructure and corrosion studies on different zones of super duplex stainless steel UNS S32750 weldment, Front Mater. 2020; 7.
[37] Gong W, Liu J, Li Y, Yang H, Liu J, Zheng S, Influence of Ce addition on microstructure and corrosion resistance of 2101 duplex stainless steel, Steel Res Int. 2021; 92(8): 2100003.
[38] Jeon S.H, Kim Y.J, Lee S.Y, Kim Y.S, Park Y.S, Effects of cerium on the compositional variations in and around inclusions and the initiation and propagation of pitting corrosion in hyperduplex stainless steels, Corros Sci. 2013; 75: 367-75.
[39] Kim S.M, Jeon S.H, Choi J.W, Lee Y.S, Effect of Si and Ce addition on the microstructure and pitting corrosion resistance of hyper-duplex stainless steels, Corrosion. 2014; 71(4): 470-82.
[40] Wang H, Liu S, Zhang Z, Chen C, Yang Z, Effects of rare earth metals on microstructure, mechanical properties, and pitting corrosion of 27% Cr hyper duplex stainless steel. Corrosion. 2022; 61(1): 873-87.
[41] Angelini E, Di Barro B, Rosalbino F, Microstructural evolution and localized corrosion resistance of an aged superduplex stainless steel, Corros Sci. 2004; 46: 1351-67.
[42] Atapour M, Shamanian M, Esmailzadeh M, Pitting corrosion susceptibility of friction stir welded lean duplex stainless steel joints, Int J Adv Manuf Technol. 2016; 83: 721-28.
[43] Zhang X, Wang Z, Li S, Lu Z, Effects of heat treatment on precipitation and corrosion resistance of cerium-containing super austenitic stainless steel S31254, Corros Commun. 2022; 8: 1-8.
[44] Jeon S.H, Hong D.H, Kim H.J, Park Y.S, Effect of Ce addition on the precipitation of deleterious phases and the associated intergranular corrosion resistance of 27Cr–7Ni hyper duplex stainless steels, Corros Sci. 2015; 90: 313-22.
[45] Fernández-Domene R.M, Seitz M, Minozzi S, Falco E, López A, Garcia-García F, Effect of alloying elements on the electronic properties of thin passive films formed on carbon steel, ferritic and austenitic stainless steels in a highly concentrated LiBr solution, Thin Solid Films. 2014; 558: 252-58.
[46] Jeon S.H, Park I.J, Kim H.J, Kim S.T, Lee Y.K, Park Y.S, Effect of Cu on the precipitation of deleterious phases and the mechanical properties of 27Cr–7Ni hyper duplex stainless steels, Mater Trans. 2014; 55: 971-77.
[47] Zhu M, Xu B, Li J, Li H, Deng Z, Yang K, Study the correlation between passive film and AC corrosion behavior of 2507 super duplex stainless steel in simulated marine environment, J Electroanal Chem. 2020; 864: 114072.
[48] Zhu M, Li H, Xu B, Li J, Yang K, Study on the microstructure and alternating current corrosion behavior of SAF2507 super-duplex stainless steel in 3.5% NaCl solution, J Mater Eng Perform. 2020; 29(2): 1366-74.
[49] Luo H, Shan H.Z, Dong C.F, Li X.G, Passivation and electrochemical behavior of 316L stainless steel in chlorinated simulated concrete pore solution, Appl Surf Sci. 2017; 400: 38-48.
[50] Rahimi E, Rahimi F, Dini M, Tan K, Gan Y, Characterization of the passive layer on ferrite and austenite phases of super duplex stainless steel, Appl Surf Sci. 2019; 496: 143634.
[51] Cheng X, Wang Y, Dong C, Li X, The beneficial galvanic effect of the constituent phases in 2205 duplex stainless steel on the passive films formed in a 3.5% NaCl solution. Corros Sci. 2018; 134: 122.
[52] Yao J, Meng D, Dong C, Passive film on 2205 duplex stainless steel studied by photo-electrochemistry and ARXPS methods, Corros Sci. 2019; 146: 221.
[53] Sahli A.A, Ghandehari E, Macdonald D.D, Effect of tungsten alloying on passivity breakdown of nickel, Mater Corros. 2019; 70: 216.
[54] Jeon S.H, Kim Y.J, Lee S.Y, Park Y.S, Passivation behavior of Ce-containing hyper duplex stainless steels in sulfuric acid solution, Mater Trans. 2015; 56(8): 1287-93.
[55] Wang L, Chen Z, Huang X, Li X, Wang Z, Quantitative analysis of local fine structure on diffusion of point defects in passive film on Ti, Electrochim Acta. 2019; 314: 161-72.